High-pressure neutron diffraction studies at LANSCE

**Yusheng Zhao · Jianzhong Zhang · Hongwu Xu · Konstantin A. Lokshin ·
Duanwei He · Jiang Qian · Cristian Pantea · Luke L. Daemen · Sven C. Vogel ·
Yang Ding · Jian Xu**

Abstract The development of neutron diffraction under extreme pressure (P) and temperature (T) conditions is highly valuable to condensed matter physics, crystal chemistry, materials science, and earth and planetary sciences. We have incorporated a 500-ton press TAP-98 into the HiPPO diffractometer at the Los Alamos Neutron Science Center (LANSCE) to conduct in situ high-P–T neutron diffraction experiments. We have developed a large gem-crystal anvil cell, ZAP, to conduct neutron diffraction experiments at high P. The ZAP cell can be used to integrate multiple experimental techniques such as neutron diffraction, laser spectroscopy, and ultrasonic interferometry. More recently, we have developed high-P low-T gas/liquid cells in conjunction with neutron diffraction. These techniques enable *in situ* and *real-time* examination of gas uptake/release processes and allow accurate, time-dependent determination of changes in crystal structure and related reaction kinetics. We have successfully used these techniques to study the equations of state, structural phase transitions, and thermomechanical properties of metals, ceramics, and minerals. We have conducted researches on the formation/decomposition kinetics of methane, CO_2 and hydrogen hydrate clathrates, and hydrogen/CO_2 adsorption of inclusion compounds such as metal–organic frameworks (MOFs). The aim of our research is to accurately map out phase relations and determine structural parameters (lattice constants, atomic positions, atomic thermal parameters, bond lengths, bond angles, etc.) in the P–T–X space. We are developing further high-P–T technology with a new 2000-ton press, TAPLUS-2000, and a ZIA (Deformation-DIA type) cubic anvil package to routinely achieve pressures up to 20 GPa and temperatures up to 2000 K. The design of a dedicated high-P neutron beamline, LAPTRON, is also underway for simultaneous high-P–T neutron diffraction, ultrasonic, calorimetry, radiography, and tomography studies. Studies based on high-pressure neutron diffraction are important for multidisciplinary sciences, particularly for theoretical/computational modeling/simulations.

1 Introduction

Neutron scattering continues to play an increasingly important role in determination of crystal structure, lattice dynamics, texture development, and magnetic excitations. It has been used advantageously to determine atomic positions and to study atomic thermal vibrations [1–3]. Neutrons interact directly with nuclei so that, unlike X-ray, scattering is independent of atomic number (Z) but can be used to differentiate isotopes of the same element. Neutron scattering factors, again unlike X-rays, do not decrease for high-index (hkl) reflections, with the consequence that much more crystallographic information can be obtained. The large Q ($= 2\pi/\lambda$) coverage of neutron diffraction allows for the detailed study of crystal structure, hydrogen bonding, magnetism, and thermal parameters of light-elements-(e.g., H, Li, and B) and heavy-elements-(e.g., Ta, U, and Pu,) bearing compounds, which are difficult to investigate using X-ray diffraction techniques [4–9]. Furthermore, neutrons are sensitive to magnetic moments of atoms and can therefore be used for studies of magnetic order–disorder, colossal magneto-resistance, and spin glasses [9, 10].

Y. Zhao (✉) · J. Zhang · H. Xu · K.A. Lokshin · D. He · J. Qian ·
C. Pantea · L.L. Daemen · S.C. Vogel
Los Alamos Neutron Science Center, Los Alamos National
Laboratory, Los Alamos, NM 87545, USA
e-mail: yzhao@lanl.gov

Y. Ding · J. Xu
Geophysical Laboratory, Carnegie Institution of Washington,
Washington, DC 20015, USA

In situ high-P variable-T (both high-T and low-T) neutron diffraction experiments provide unique opportunities to study materials under extreme conditions. The high penetrating power of neutrons presents great advantages in designing pressure cells with various kinds of high strength metals, alloys, and ceramics. Some extremely difficult studies, e.g., Debye–Waller factor as a function of pressure and temperature, can only be derived using in situ high-P neutron diffraction techniques. High-P neutron diffraction realizes its full potential in a broad spectrum of scientific problems. For instance, puzzles in earth science such as the global carbon cycle and the role of hydrous minerals for water exchange between lithosphere and biosphere can be directly addressed [11, 12]. The pressure and temperature effects on hydrogen bonding in ice, hydrates, and hydrocarbon phases can only be refined using high-resolution neutron diffraction [13, 14]. The uniqueness of neutron diffraction in resolving pair-distribution-functions can advance the study of liquid, melts, and amorphous phases under high-P variable-T conditions [15, 16]. Moreover, by introducing in situ shear and/or differential stress, the yield strength and texture development of metals and minerals accompanied with phase transitions at high-P–T conditions can be studied by in situ neutron diffraction [17–22]. This review article summarizes our recent instrument developments and research activities done at Lujan Neutron Scattering center of LANSCE.

2 High-pressure instruments

With the development of the toroidal anvil press, significant progress has been made regarding neutron diffraction experiments at high pressure, as pioneered by the Paris–Edinburgh (P–E) group [23–30]. The new capacity to conduct neutron diffraction experiments simultaneously at high pressure and high temperature has extended the scope of possible investigations. Zhao et al. [31, 32] and Le Godec et al. [26] have overcome severe difficulties and made the cell assemblies work effectively under simultaneous high-P–T conditions. Although high-P variable-T neutron diffraction experiments are inevitably faced with challenging issues, such as needs for large sample volumes, long data collection times, and wide detector areas, we have developed a number of high-pressure instruments and cell assemblies and successfully conducted high-P variable-T neutron diffraction experiments at LANSCE. We have achieved simultaneously high pressures and temperatures up to 10 GPa and 1500 K [31, 32] as well as low temperatures down to 4 K at pressures up to 1 GPa [33]. With an average of 4–6 hours of data collection, the diffraction data are of sufficiently high quality for the determination of structural parameters and thermal vibrations using the Rietveld method [28].

We have studied metals, ceramics, minerals, clathrate hydrates, and MOFs using these neutron diffraction techniques [11, 13, 14, 18, 34, 35].

2.1 TAP-98: a high-pressure press designed for HiPPO

A time-of-flight (TOF) neutron diffractometer, HiPPO, for materials studies has been designed, constructed, and operational at LANSCE [36–38]. The HiPPO diffractometer takes advantage of the improved spallation neutron source at LANSCE and a short flight path to achieve a high neutron flux at the sample of 10^8 n/cm^2/s, nominally. The three-dimensional detector banks consist of about 1,400 ^{3}He gas-filled detector tubes and allow collection of diffracted neutrons in virtually all directions in space. The HiPPO beamline increases more than five times the detector area for the $2\theta = 90°$ diffraction banks (*used mostly for high-pressure experiments*) compared to the old HIPD beamline.

To fully utilize the capabilities of the HiPPO diffractometer, we designed a toroidal anvil press, TAP-98, better adapted to HiPPO for neutron diffraction at high pressures and temperatures [31, 32]. The press design has a loading capacity of 5.0 Mega-Newton (500 metric ton). The compact size of the TAP-98 loading frame, 71.12 cm × 53.34 cm × 17.78 cm (28″ × 21″ × 7″), is custom-tailored/trimmed to fit into the HiPPO sample chamber, which has a rim opening of 73.66 cm (29″). The dual-plate frame in a split arrangement allows incident neutrons to have multiple access beam ports. The composite curvature window opening minimizes the stress concentration and maximizes the detection of the diffracted neutrons. Specifically, the design of TAP-98 with an open rectangular window reduces the shadow angles to 110° (a 29% reduction), and, at the same time, the anvils with a slope of 10° fully use the 90° diffraction banks. The design of the TAP-98 press and anvils has an increased diffraction detecting area, about 158% compared with the PE cell when used on HiPPO. The enlarged tooling space of about 4,916 cm^3 (∼300 cubic inches) allows easy installation of high-temperature and high-magnetic field attachments to the cell assemblies.

For the high-pressure anvil design, we used electric-discharge machining (EDM) to carve the toroidal profile on the "front-side" of the polycrystalline diamond (PCD) die-blank sintered in a tungsten carbide cylinder (De Beer, SYNDIE). The toroidal profile, first proposed by Khovstansev et al. (1977) [39], is designed to have all revolving circles tangential to each other so that the concave and convex portion of the toroids will have no stress concentration spots (Fig. 1 Left). The "back-sides" of the top and bottom anvils are carved differently: the top anvil has a hemispherical dome-shaped dip for less attenuation of the incident neutron beam, whereas the bottom anvil has a through-hole to allow a ceramic tube for the thermocouple shielding to enter
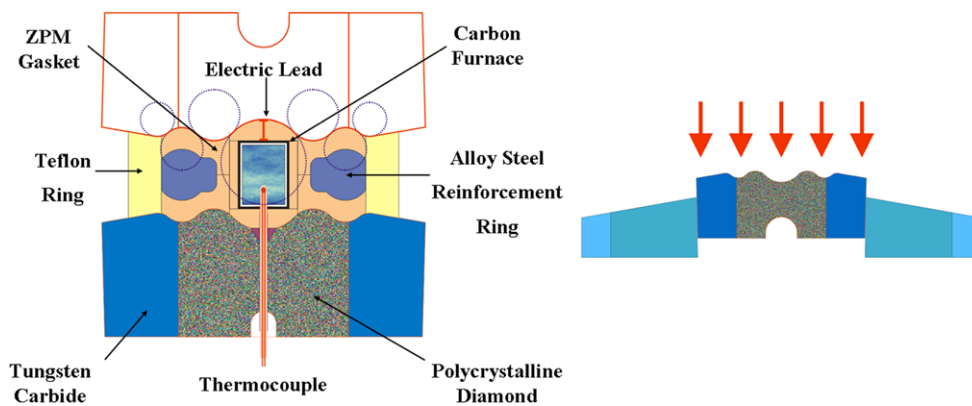
Fig. 1 Key elements of the anvil-cell assembly package. *Left*: the toroidal profiles formed by revolving circles tangential to each other result in no stress concentration at the concave and convex portions of the anvils. This drawing shows an early design of the cell assembly with super-alloy reinforcement rings being sandwiched between two ZPM ceramic gaskets. *Right*: the pushed-in ($F = 10$–15 ton) assembly of the toroidal anvil (with a tapered angle of 1.5°, i.e., an enclosed angle of 3°) into a hardened steel ring

the sample. A cone-shape dent is carved at the center of the bottom anvil so that a deformed stainless steel cone under pressure can grasp the thermocouple tube to prevent its extrusion. A tapered angle of 1.5° (an enclosed angle of 3°) is cut on the side of the tungsten carbide (WC) cylinder with a two-thousandth diameter-interference to the center hole of the hardened steel (50 HRc, VascoMax C-300) reinforcement ring (Fig. 1 Right). The PCD anvil is pushed into the steel reinforcement ring with a load of 10–15 tons; the corresponding confining pressure acting upon the PCD piece is approximately 400 MPa. A 10° slope is cut on the WC portion of the anvil, and it extends all the way to the hardened steel reinforcement ring to allow diffracted neutrons access to an enclosed 20° of axial aperture window.

Our gasket development is built upon the success of our high-P–T cell assembly for the P–E cell. Machinable ZPM (zirconium phosphate) ceramic material with low thermal expansivity (0.9×10^{-6}/K, ~1/8 of alumina and ~1/15 of magnesia) and low thermal conductivity (0.8–0.9 W/m · K, ~1/5 of alumina and ~1/60 of magnesia) is used in the high-P–T cell assembly. The thermomechanical and neutron "transparency" properties of the ZPM ceramic make it an ideal gasket material for high-P–T neutron diffraction experiments. We have tested three gasket setups: (1) whole ZPM ceramic gasket; (2) ZPM gasket sandwich with a steel reinforcement ring (Fig. 1 Left); and (3) alloy steel gasket sandwich with a lithographic disk (Fig. 2). The first one exhibits the best performance at high pressure, but the sample deforms significantly from a cylinder into a disk shape after pressurization, and the remaining diffraction window between the top and bottom anvils is rather small (<1.0 mm). The second one can keep a better sample shape after the application of pressure, but it occasionally shorts out the electric heating circuit. The third one performs better than the others in terms of sample shape, insulation, and access for the diffracted neutron beam.
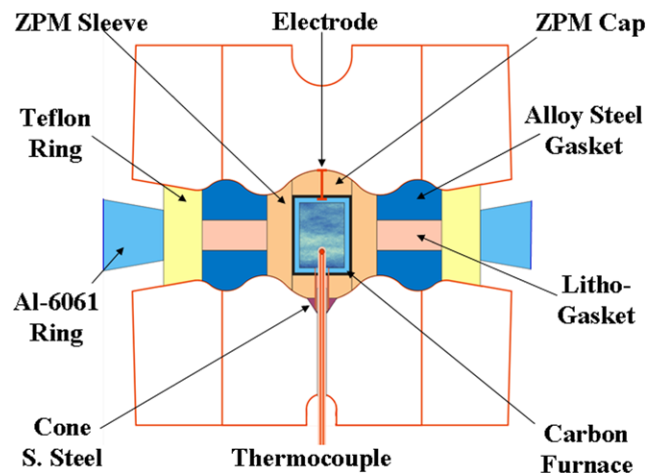

Fig. 2 Cell assembly used in high-P–T neutron diffraction experiments. The sample has a total length of 6–8 m and is located at the center of the carbon furnace. The sample diameter is 4 mm for a metallic sample for which an electrical insulation sleeve made of NaCl is needed; the sample diameter is 5.5 mm for insulating samples

We use a teflon ring to confine the ceramic/lithographic gasket and to avoid electrical shorting-out at high-P–T conditions. It stretches/elongates and survives at reasonably high temperatures and is "transparent" to neutrons. We added an Al-6061 confining ring, which is strong, tough, and expandable, to reinforce the gasket assembly for high-P–T neutron diffraction experiments. It also enhances pressure efficiency quite notably. We keep the tubular furnace design, consisting of a cylindrical carbon sleeve and two flat carbon disks, for its advantage of homogeneous temperature distribution. Amorphous carbon is used as furnace material to reduce the contamination of the diffraction pattern with graphite Bragg peaks and to attenuate the mechanical instability of the furnace caused by the slippery nature of graphite. The cylinder/disk carbon furnace does not have di-

rect contact with the anvils, and the electric circuit is completed by thin platinum wires and foils (cross sectional area $\sigma \sim 0.3$ mm^2). The cylinder/disk carbon furnace is encapsulated in a low thermal conducting ceramic, ZPM sleeve and ZPM caps, for electrical and thermal insulation. Thin platinum foils are placed on the polycrystalline diamond anvils to make the electrical connections extend to the WC portion of anvils.

A straight-through thermocouple with ceramic shielding tube is mounted through the central hole of the bottom anvil. This configuration has the minimum deviatoric stress acting upon the thermocouple, thus increasing its survivability. We often use thermocouples made of stronger W/W–Re wires and have achieved high success rate in temperature measurements at high pressure. The front side of the top and bottom anvils is painted with a Gd_2O_3 paste to block unwanted neutron scattering from anvil materials; a hole lets the incident neutron beam pass through. The front anvils and the cell assembly are packaged together after sample loading. The package is then placed inside TAP-98 between two tungsten carbide back anvils.

With the described anvil and pressure-cell designs, we have successfully conducted high-P–T neutron diffraction experiments using TAP-98 at LANSCE and achieved simultaneously high pressures and temperatures up to 10 GPa and 1500 K on large samples with a volume of about 150 mm^3. The temperature variation over a time period of several hours and as measured by the thermocouple is mostly within ±10 K at temperatures of 1000 to 1500 K. The sample pressure can be determined using the diffraction lines of pressure calibrants (such as NaCl, CsCl, and MgO) and their well-determined thermoelastic equations of state, with the known sample temperature.

2.2 ZAP cell: a moissanite anvil high-pressure cell

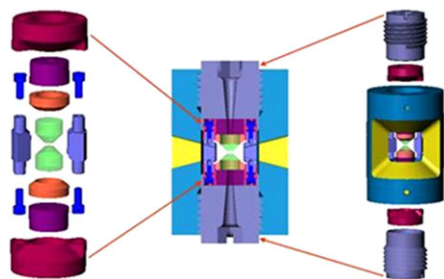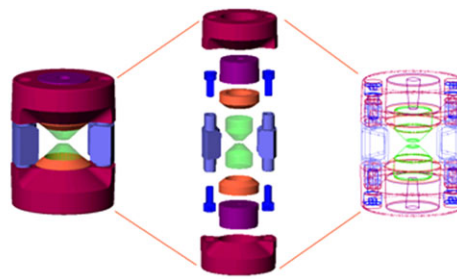Our recent development of the ZAP cell using the opposing single-crystal moissanite (SiC) anvils provides much larger window-openings and multiple mounting orientations for neutron diffraction and for future low-temperature and tomography studies at high pressure. The transparent gem-quality moissanite anvils also allow us to perform laser spectroscopy studies and ultrasonic interferometry together with neutron diffraction. The key features of this new anvil cell design are: *to lock-up* pressure on an easily loaded inner anvil cell with a robust piston-cylinder alignment loading; *to disengage* the high-pressure anvil setting from the bulky hydraulic ram and loading frames; and *to enlarge* diffraction windows for better coverage of crystal reciprocal space. The ZAP cell can be loaded to high pressures with a hydraulic press and then mounted on a goniometer so that powder and single-crystal diffraction experiments can be performed. The major components of the ZAP cell (Fig. 3) are: (1) a Merrill–Bassett cell at central core for its simplicity of design and ease of sample loading; (2) Mao–Bell cell's piston-cylinder anvil design for its excellent alignment in compression; (3) clamped cell's load-releasing feature and pressure maintaining capability after clamping; (4) cylindrical cell's window opening arrangement for its wide coverage in reciprocal space; (5) Paris–Edinburgh press' central plug with a heavy-duty screw/thread to work against hydraulic force; and (6) TAP-98 press' split loading frame to maximum neutron beam access.

We have also designed a self-aligned and bolt-assembled inner cell with gem-quality moissanite (SiC) single crystals as the anvils (Fig. 3 Left) to apply pressure to much smaller sample volumes (<30 mm^3). It is the inner part of a lock-up portable ZAP cell. The inner cell can be readily fitted into the TAP-98 press and loaded to high pressure with the P–T control system for TAP-98. The highest pressure achieved to date using the gem SiC anvils is 20.3 GPa [40] with a much smaller sample size of 20 mm^3.

2.3 High-pressure/low-temperature gas/liquid cells

Neutron diffraction in conjunction with high-pressure/low-temperature capabilities is a powerful tool in tackling many

Fig. 3 (*Left*) Major components of the ZAP cell designs. To lock up pressure, the two pistons are oppositely threaded (*CW & CCW*) to serve as "bolts," while the outer cylinder body serves as the turnbuckle "nut," with a small gap for advance of the pistons. An aluminum or TiZr ring is used as the gasket. (*Right*) Exploded view of a self-aligned, bolt-assembled room-temperature inner cell with gem-quality moissanite single crystals as the anvils. This inner cell is loaded in the ZAP cell (*Left*) and it is designed for achieving pressures up to 20 GPa
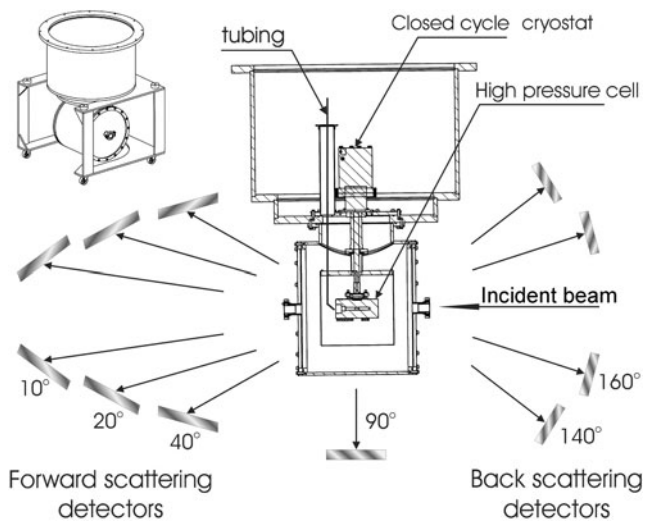
Fig. 4 Schematic general view (*in the top-left corner*) and the enlarged sectional view of the experimental setup designed for in situ high-P low-T neutron diffraction at LANSCE's HIPPO beamline

scientific problems (such as magnetic ordering, phase transformation, and chemical reaction) in condensed matter physics, materials, energy, and earth and planetary sciences [41–44]. In particular, the use of a fluid (gas or liquid, such as helium) as the pressure-transmission medium can produce the ideal hydrostatic conditions, thereby eliminating the deviatoric stress effect that commonly occurs in an anvil-type pressure cell with a solid pressure medium. In some cases, the fluid can also act as a reactant, allowing in situ studies of the structural and kinetic mechanism of the reaction or interaction between the fluid and the studied material. For example, in the hydrogen adsorption experiments of meta-organic frameworks (MOFs), deuterium gas D_2 (instead of H_2 gas to avoid the large incoherent scattering of neutrons by hydrogen) is not only a species of interest but also acts as the pressure-transmitting medium.

We have developed a horizontal-type gas/liquid pressure cell to perform high-P low-T neutron scattering experiments at HIPPO and other beamlines at LANSCE (Fig. 4) [33]. Particularly, this pressure cell takes the full advantages of HIPPO, which covers a wide range of Q (0.13–52.4 Å^{-1}) values with multiple detectors at different diffraction angles. The cell is constructed of Al-7075 alloy since aluminum has a small cross section for neutron scattering, and it maintains reasonably high strength under high pressure. The horizontal alignment of the cell relative to the incident neutron beam results in a large separation (2–4 cm) of the sample, which is in the middle of the cell, from the cell ends, thereby allowing effective shielding of the parasitic scattering from the cell. The cell is pressurized with a Harwood gas/fluid pressure intensifier via thin high-pressure tubing. It is attached to a closed-cycle cryostat and surrounded by two temperature shields. The cryostat stands on the HIPPO cover, which

can be moved and used off-line for testing and preparation procedures. This fluid cell can hold pressures up to 10 kbar and maintain temperatures down to 4 K on samples as large as 10 cm^3.

In addition to the above pressure cell, we have developed several cylindrical vertical-type gas/liquid cells with various desired maximum pressures using different materials (V, Al, etc.). For many energy and environmental applications, pressure capabilities in the order of tens or hundreds of bars can be very useful. For instance, storage of hydrogen in a MOF typically requires a pressure in the order of 100 bar or lower, as higher pressure will consume significant amounts of energy, making its use economically unfeasible. Thus we have designed and manufactured several lower-pressure cells in conjunction with gas-loading capability, which allows measurement of the amount of gas loaded into the pressure cell. Coupled with the high counting rate and wide Q range of HIPPO, these cells are thus ideal for in situ time-resolved neutron diffraction studies of materials at various pressure and temperature conditions.

3 Case studies using high-P variable-T neutron diffraction

Over the past several years, we have successfully applied the techniques described in Sect. 2 to determine the equations of state, structural, and magnetic phase transitions and thermo-mechanical properties of metals, ceramics, and minerals under high-pressure and/or high-temperature conditions. We have also conducted researches on the formation/decomposition of methane, CO_2 and hydrogen clathrate hydrates, and hydrogen/CO_2 sorption/desorption of MOFs. The aim of the later research is to accurately map out phase diagrams of these important gas-storage materials and to determine their structural parameters and phase stability in the $P–T–X$ space. Summarized in this section are some typical examples of our recent research activities, performed at the HIPPO beamline of LANSCE.

3.1 Thermo-mechanical properties of nanocrystalline nickel

Based on high-$P–T$ time-of-flight neutron and synchrotron X-ray diffraction, we have developed an analytical method for deriving thermo-mechanical properties of polycrystalline materials under high-pressure and high-temperature conditions [20, 22]. This method deals with the nonuniform stress among the heterogeneous crystal grains as well as grain-boundary strain in nanocrystalline materials by examining the peak width variation at different $P–T$ conditions. Because the method deals with the lattice d-spacing and the local-stress-caused deformation directly, it can be used for

Fig. 5 Apparent stresses for nano-Ni and micron-Ni plotted as functions of pressure and temperature
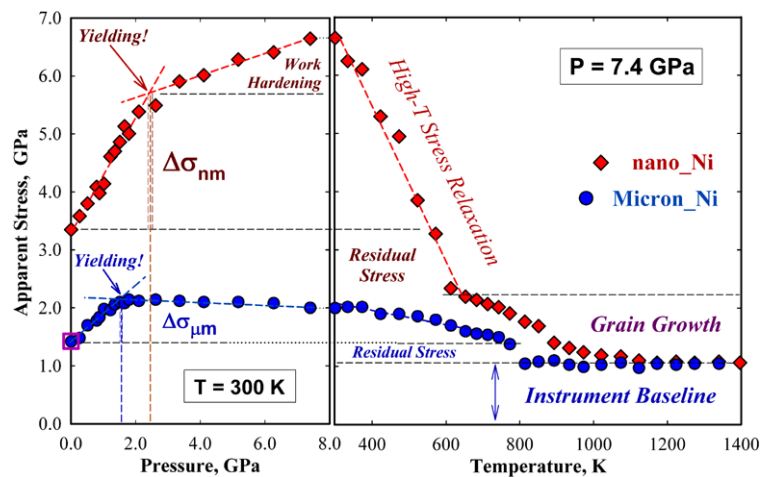
analyzing any diffraction profile, independent of detecting modes. We also developed a correction routine using diffraction elastic ratios to deal with the severe grain boundary strain and/or strain anisotropy effects related to nanoscale grain sizes, so that the significant data scatterings can be straightened in a physically meaningful way. We have applied these methods to study thermo-mechanical properties of bulk and nanocrystalline nickel.

Figure 5 shows the derived apparent stresses as functions of pressure and temperature for nano-Ni and micron-Ni. The derived yield stress of high-*P triaxial compression* is $\Delta\sigma_{yield}^{nm} \approx 2.35$ GPa for the nano-Ni, which is similar to the uniaxial tensile strength of 2.25 GPa determined by Budrovic et al. [45]. The corresponding bulk yield stress (*compression*) of micron-Ni is $\Delta\sigma_{yield}^{\mu m} \approx 0.75$ GPa, about a factor-of-three smaller than that of nano-Ni. These observations are consistent with the classic Hall–Petch law [46, 47], which indicates a significant increase in materials strength as grain size decreases to the nanometer scale.

The simple approach of Fig. 5 can identify micro/local yield at the grain-to-grain interactions due to high stress concentration and macro/bulk yield of the plastic deformation over the entire sample. It is also capable of revealing grain growth, work hardening and work softening, and thermal relaxation under high-*P*–*T* conditions, as well as the intrinsic residual or grain boundary strain in the polycrystalline bulks. In addition, our approaches allow the instrumental contribution to be illustrated and subtracted in a straightforward manner, thus avoiding the potential complexities and errors resulting from the instrument correction. For example, at $T > 1,100$ K, the high-temperature data show a complete merging of nano-Ni and micron-Ni in terms of stress or strain levels, indicating that the corresponding apparent strain is due to the instrument resolution, and there are no effects of microstrain and grain size in this stage. This graphic derivation is important not only for a comprehensive understanding of constitutive behaviors but also for the correct application of the peak-profile analysis method.

Figure 6 shows the apparent stress determined using our method and dislocation density derived from the Ungar model using neutron diffraction data of nano-Ni at atmospheric pressure, along with grain size derived by both methods. It is evident that the two methods give rise to comparable results for the grain-size analysis, in both absolute values and their variations with temperature. The dislocation densities derived from the Ungar method also show the same trends of variation with temperature as the grain boundary strains we derived. Based on Ashy [48] and Ashby and Jones [49], the dislocations in plastically deformed crystals can be separated into "geometrically necessary" dislocations (those associated with the existence of grain boundaries) and "statistically stored" dislocations (glissile dislocations participating in the plastic deformation). In the Ni nanocrystals, these two different types of dislocations correlate with the grain size variation [50]. In the Ungar method the dislocation density is a parameter that characterizes the grain boundary or residual strains caused by crystalline dislocations. Therefore, although it is not parametrically equivalent to the grain boundary strain we determined, both of them describe similar physical performances of Ni nanocrystals.

3.2 Equation of state of lithium deuteride

With a rock salt structure (B1) and only four electrons per unit cell, lithium hydride (LiH and its isotopic analogue LiD) is the simplest ionic crystal in terms of electronic structure. The low mass of the constituent atoms in LiH and LiD make them ideal candidates for calculation of the zero-point motion contribution to the lattice energy.

Thermal expansion, equation of state (EOS), and phase stability are fundamental properties of condensed matter. We conducted neutron diffraction experiments on LiD at pressures up to 4.2 GPa and temperatures up to 1,386 K [51]. We also conducted thermal expansion measurements at ambient pressure. The experimental results (Figs. 7 and 8) allow

Fig. 6 Comparison of the results of the peak-profile analysis between our approach and the Ungar approach [50] for nanocrystalline nickel
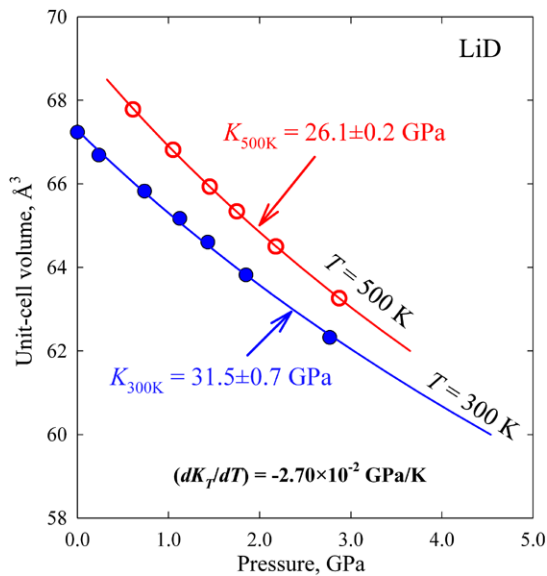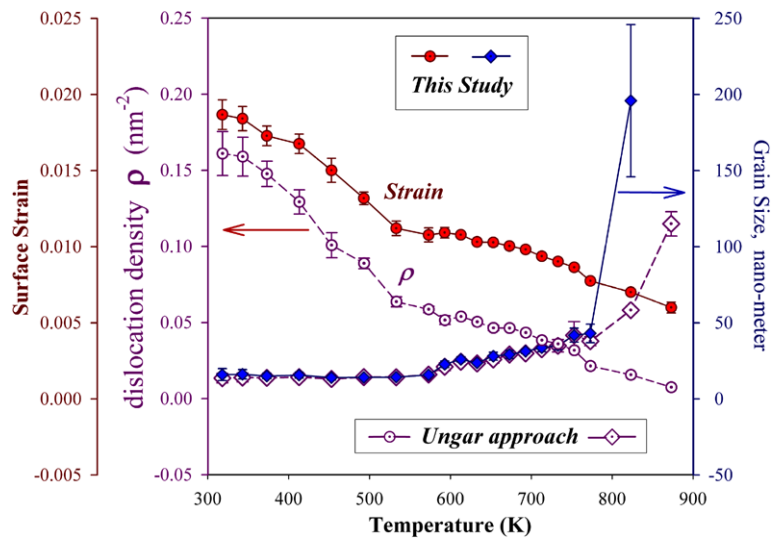

Fig. 7 Pressure–volume–temperature data measured for LiD using time-of-flight neutron diffraction. The extrapolated zero-pressure volume from the 500 K isotherms is shown in Fig. 8

Fig. 8 Volume–temperature data at atmospheric pressure (*solid squares*) and 3.0 GPa (*solid circles*) of LiD. The 3.0 GPa data were corrected based on the high-T data measured at pressures of 2.8–4.1 GPa and the $P-V$ isotherms shown in Fig. 7. The zero-pressure volume extrapolated from the 500 K $P-V$ isotherms is in good agreement with the measured data

us to determine the thermoelastic properties of LiD, such as the pressure dependence of thermal expansivity and the temperature derivative of bulk modulus. These thermoelastic parameters were derived using a Birch–Murnaghan equation of state. With the pressure derivative of the bulk modulus, K_0', fixed at 4.0, we obtained: ambient bulk modulus $K_0 = 31.5 \pm 0.7$ GPa, temperature derivative of bulk modulus at constant pressure $(\partial K/\partial T)_P = -2.7 \times 10^{-2}$ GPa/K, volumetric thermal expansivity $\alpha_T (\text{K}^{-1}) = 9.8 \pm 0.71 \times 10^{-5} + 12.62 \pm 1.09 \times 10^{-8} T$ at atmospheric pressure and $\alpha_T (\text{K}^{-1}) = 5.45 \pm 1.17 \times 10^{-5} + 6.53 \pm 1.45 \times 10^{-8} T$ at 3.0 GPa, and the pressure derivative of thermal expansion $(\partial \alpha/\partial P)_T = -2.72 \times 10^{-5}$ GPa^{-1} K^{-1}. Within the experimental uncertainties, the ambient bulk modulus and volu-
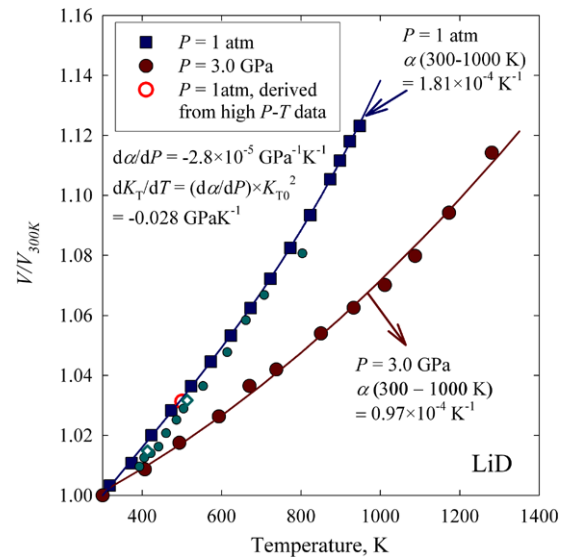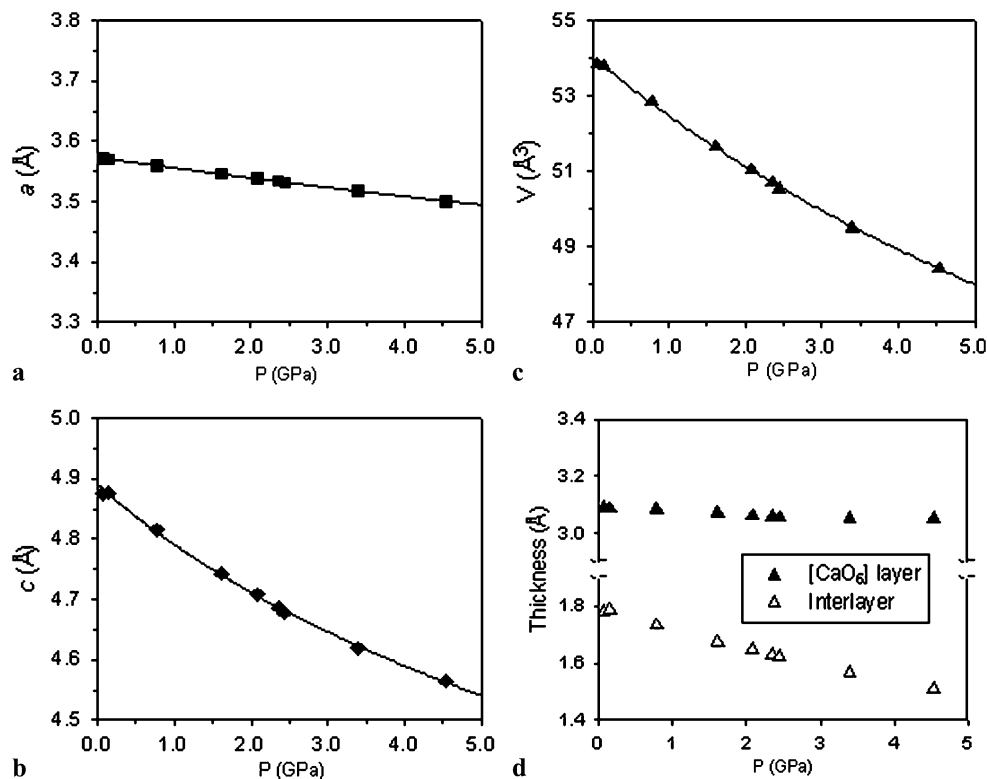
metric thermal expansion determined from this work are in good agreement with previous experimental results, whereas the derived $(\partial K_T/\partial T)_P$ and $(\partial \alpha/\partial P)_T$ values have been determined for the first time.

3.3 Compressibility and H-bonding behavior of simple hydroxides

Interests in hydrous minerals, which may store water in the Earth's mantle, have inspired numerous high-P–T stability studies of simple hydroxides, M(OH)$_2$, where M = Mg, Ca, Ni, Co, Mn, etc. [52]. These hydroxides possess a CaI$_2$-type

layered structure (space group $P\bar{3}m1$), in which [MO$_6$] octahedra are linked via edge-sharing into layers normal to the c axis and H atoms that are bonded to O to form hydroxyls, situated between the [MO$_6$] layers. Though uncommon in the deep Earth, M(OH)$_2$ hydroxides are present as component units in the structures of complex hydrous minerals, potential hosts for mantle water. Thus studying the structures and phase equilibria of simple hydroxides at elevated pressure and temperature provides insights into mechanisms of water storage in the Earth's interior.

We have performed high-P–T experiments on several simple hydroxides including deuterated brucite Mg(OD)$_2$, portlandite Ca(OD)$_2$ [11], and Ni(OD)$_2$. Rietveld analysis of the neutron data allows determination of their structural parameters as functions of pressure and temperature. For example, Figs. 9a–9c plot unit-cell parameters of Ca(OD)$_2$ with pressure. With increasing pressure, both a and c decrease, and thus cell volume V also decreases. Fitting the volume data to the third-order Birch–Murnaghan EOS (Fig. 9c) yielded $K_0 = 32.2 \pm 1.0$ GPa and $K_0' = 4.4 \pm 0.6$, which are in reasonably good agreement with previous measurements using synchrotron X-ray and neutron diffraction (e.g., [53, 54]). Although both a and c decrease with increasing pressure, the rate of contraction in c is much larger than that in a (Figs. 9a and 9b). Fitting the a and c data to the one-dimensional form of the third-order Birch–Murnaghan EOS yielded $K_a = 70.5 \pm 1.9$ GPa, $K_a' = 1.6 \pm 1.0$ and $K_c = 15.3 \pm 0.9$ GPa, $K_c' = 3.3 \pm 0.6$. In other words, the

c-axis is about 4–5 times more compressible than a. This anisotropic behavior is consistent with the weak H-mediated interactions within the interlayer (between [CaO$_6$] layers) and thus the ease of changing the interlayer thickness (relative to changing the [CaO$_6$] layer thickness) along c (Fig. 9d).

The shrinking of the interlayer spacing in Ca(OD)$_2$ must be coupled with changes in the interactions of D, which resides between the [CaO$_6$] layers, with O and other D. Specifically, with increasing pressure, while the O–D bond length shows little change (Fig. 10a; the slight increase above 3.4 GPa is consistent with a down-shift of the corresponding infrared frequency with increasing pressure [55, 56]), D–D, the distance between the three equivalent sites over which D is disordered increases (Fig. 10b). This behavior suggests a pressure-induced D disorder, as occurs in brucite [57]. However, the D in portlandite appears to be more disordered than that in brucite, as evidenced by its larger D–D distances, especially above ~3 GPa. The more rapid increase in the degree of D disorder in portlandite with increasing pressure may eventually result in its amorphization above ~11 GPa [56], which does not occur in brucite. Correspondingly, the D···O attraction, which operates between a given D and its closest O from the adjacent [CaO$_6$] layer, becomes strengthened, as manifested by the decrease in D···O distance (Fig. 10c). A similar trend is seen in the variation of D···D (Fig. 10d), the distance between the two nearest nonbonded D atoms associated with two neighbor-

Fig. 10 Variation of interatomic distances (**a**) O–D, (**b**) D–D, (**c**) D$\cdots$O and (**d**) D$\cdots$D in Ca(OD)$_2$ as a function of pressure
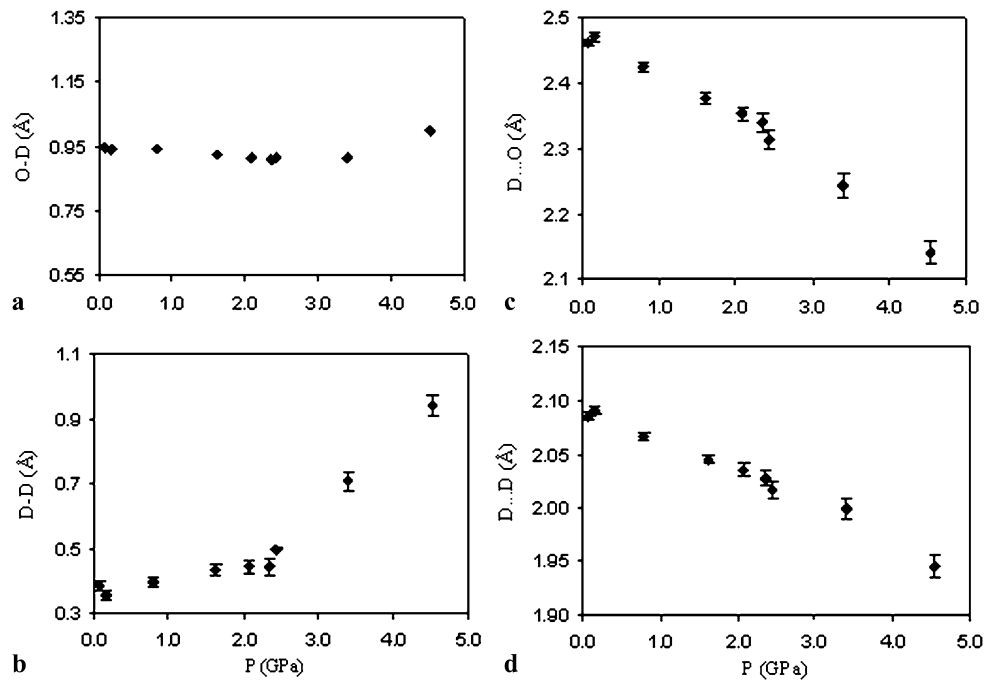
ing [CaO$_6$] layers. In other words, both the attractive D$\cdots$O and the repulsive D$\cdots$D interactions become strengthened with increasing pressure. Hence, the variations in these interatomic interactions with pressure result in the corresponding changes in the interlayer thickness, which in turn cause changes in the c dimension and anisotropic nature of the portlandite contraction.

3.4 Pressure-induced magnetic ordering and lattice distortion in 3D transition metal oxides

The 3D transition metal oxides are the simplest representatives of highly correlated electron systems and have traditionally been used for testing band structure calculations. Studies of these oxides are of fundamental importance in diverse fields ranging from condensed-matter physics and chemistry to earth science. The properties of these compounds are complicated by the interactions of charge, spin, lattice, orbital moment, and defects in the system.

FeO and CoO are paramagnetic insulators with a rock salt structure above their Néel temperatures (T_N), 198 K and 290 K, respectively. Below T_N, they transform into antiferromagnetic states. CoO distorts into a tetragonal symmetry accompanied by a small rhombohedral distortion, whereas FeO distorts into a rhombohedral structure. Upon compression at room temperature, FeO and CoO were observed to distort into rhombohedral structures at $\sim$15 GPa [58] and 43 GPa [59], respectively. It has also been observed that T_N increases in CoO and FeO upon compression [60, 61]. Based on the linear pressure dependence of T_N and its similarity to the lattice distortion at low temperature, Yagi et al. proposed

that the rhombohedral lattice distortion in FeO at $\sim$15 GPa should be associated with a magnetic ordering transition due to magnetoelastic coupling [58].

To examine the possible existence of long-range magnetic ordering in the high-pressure rhombohedral phase of Fe$_{1-x}$O wüstite, we conducted neutron diffraction measurements up to 20.3 GPa using a large-volume moissanite anvil cell at room temperature [62]. Low-temperature ambient pressure neutron measurements on the same sample were also conducted at 190, 180, and 85 K to compare with the high-pressure results. Plotted in Figs. 11 and 12 are neutron diffraction patterns collected at different pressures and different temperatures, together with the calculated patterns.

Consistent with previous experiments, we observed the magnetic peaks at 180 K under ambient pressure. However, at the highest pressure (20.3 GPa) of our experiments at 300 K, which is above the critical pressure for a cubic to rhombohedral lattice distortion, no magnetic peaks were evident in the diffraction pattern of Fe$_{1-x}$O. The absence of magnetic peaks indicates the absence of long-range magnetic order in Fe$_{1-x}$O under these conditions. This result also indicates the need to modify previously reported P–T phase diagrams of this material, as well as a reconsideration of magnetoelastic coupling between phonons and the magnetic subsystem of FeO as the driving force for the 15 GPa phase transition.

To further investigate the possible correlation between the magnetic ordering and the high-P transition in 3D transition metal oxides, we performed neutron experiments of CoO up to 9.0 GPa [62]. Plotted in Fig. 13 are neutron diffraction patterns collected at ambient pressure, 4.1 GPa, and

on the sample recovered after the pressure was released. Figure 14 emphasizes the relative intensity changes of magnetic peak $M2$ and nuclear peak 200, as a function of pressure. Above 2.6 GPa, the magnetic peaks $M1$, $M2$, $M3$, and $M4$ are first observed, indicating the occurrence of a long-range magnetic ordering transition at high pressure. Such
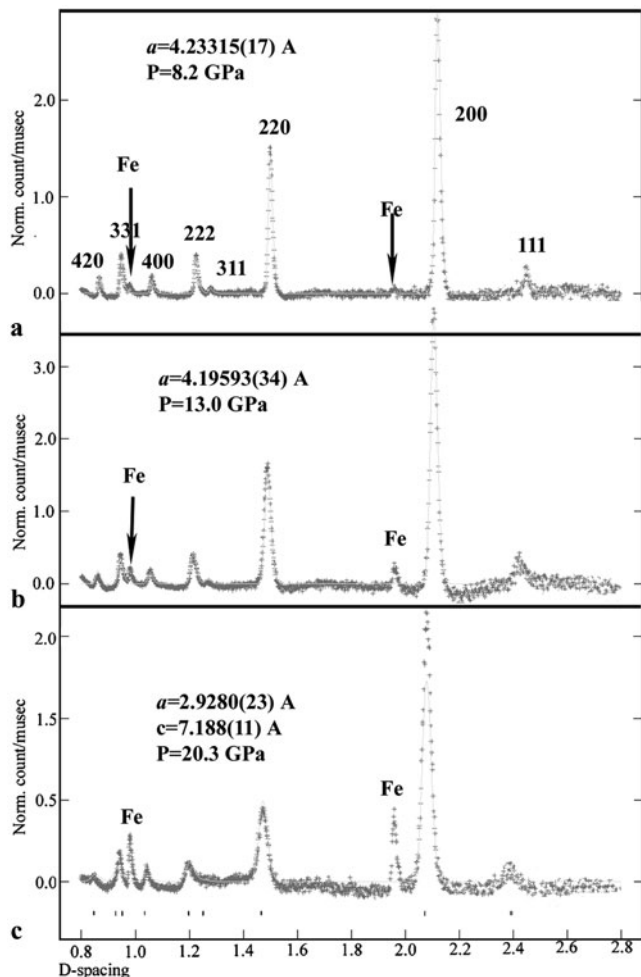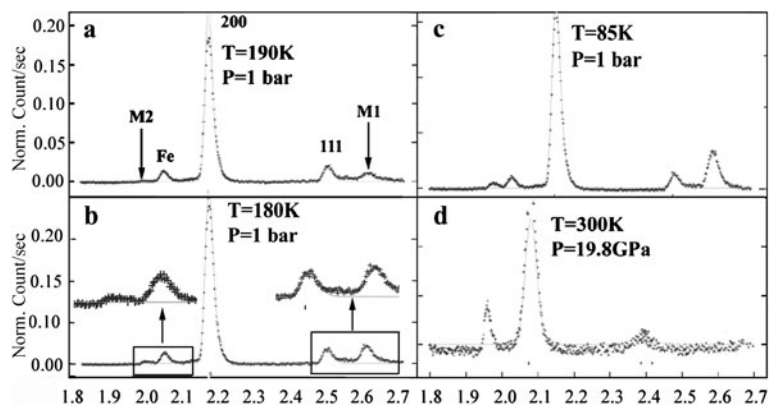

Fig. 11 Neutron diffraction patterns of $Fe_{1-x}O$ wüstite collected at (**a**) 8.2 GPa, (**b**) 13.0 GPa, and (**c**) 20.3 GPa

a transition was corroborated by a continuous increase in the relative intensity ratio of the magnetic peaks to the nuclear peak 200 with increasing pressure. After the pressure was released to ambient conditions, all magnetic peaks disappeared, indicating that the magnetic ordering transition is reversible. By fitting the intensity ratio of magnetic peak $M2$ and peak 200 as a function of pressure, the paramagnetic–antiferromagnetic ordering transition pressure was determined to be 2.2 GPa at room temperature (Fig. 14g). Thus the T_N rate of increase with pressure is 4.5 K/GPa, comparable with previous results [63]. Moreover, structure analysis with GSAS indicates that this magnetic structure is type-II antiferromagnetic. High-resolution synchrotron X-ray diffraction, however, shows no evidence of a tetragonal lattice distortion in CoO in the magnetically ordered phase. This result demonstrates that the tetragonal lattice distortion occurring with magnetic ordering in the low-temperature structure of CoO could be associated with cooperative Jahn–Teller effects-orbital ordering, which, however, are decoupled from magnetic ordering under high pressure. Hence, our high-pressure results on $Fe_{1-x}O$ and CoO demonstrate the complexity between magnetic ordering and lattice distortion, which could arise from the interplay of spin, orbital, charge, and the lattice in these strongly correlated systems [64] under high pressure.

3.5 Crystal structures and kinetics of formation/decomposition of hydrate clathrates

Clathrate hydrates are ice-like crystalline solids in which gas molecules are physically encapsulated in the frameworks bonded by water molecules that are stable typically at high-P and/or low-T conditions. Because these compounds are composed mainly of light elements (H, O, C, etc.), in situ neutron scattering is a preferred technique (compared with X-ray diffraction) for studying their structures and kinetics of formation/decomposition. Using the gas/liquid pressure cells, we have performed neutron diffraction experiments on methane–ethane, CO_2, and hydrogen clathrate (see below) hydrates [13, 14, 65, 66].
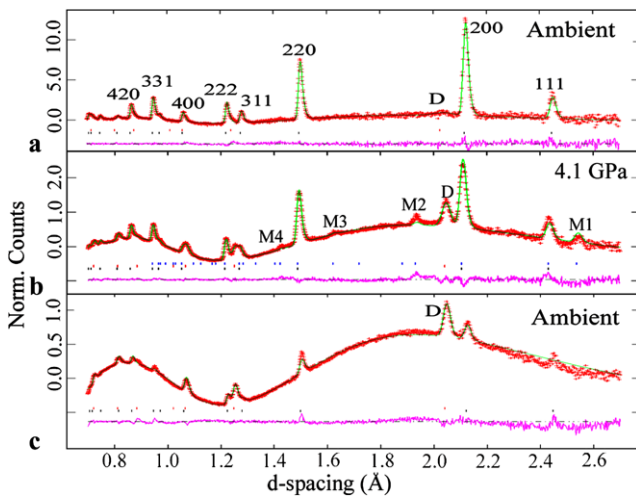
Fig. 12 Comparison of neutron diffraction patterns from 1.8 to 2.7 Å collected at (**a**) 190 K, (**b**) 180 K, (**c**) 85 K at ambient pressure, and (**d**) at 20.3 GPa and 300 K. The *solid lines* represent the calculated patterns from GSAS without magnetic ordering. $M1$: magnetic peak which has half the d-spacing of the nuclear peak (311) and can be indexed as 3/2, 1/2, 1/2; $M2$: magnetic peak with half the d spacing of (331) and can be indexed as 3/2, 3/2, 1/2

Fig. 13 Neutron diffraction patterns of CoO collected at (**a**) ambient pressure (lattice parameter $a = 4.261$ Å), (**b**) 4.1 GPa (lattice parameter $a = 4.230$ Å), and (**c**) ambient pressure (released from 9.0 GPa). M: magnetic peak; D: diamond peak
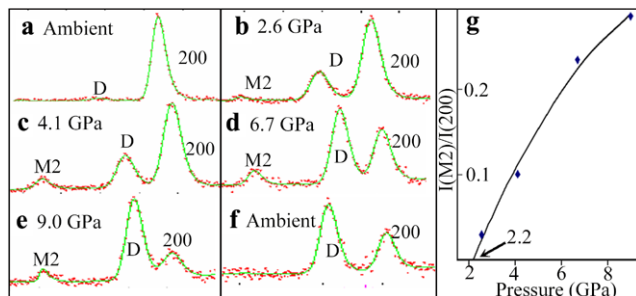

Fig. 14 The enlarged diffraction patterns consisting of magnetic peak $M2$ (3/2, 3/2, 1/2) and nuclear peak 200 at (**a**) ambient pressure, (**b**) 2.6 GPa, (**c**) 4.1 GPa, (**d**) 6.7 GPa, (**e**) 9.0 GPa, and (**f**) ambient pressure (released from 9.0 GPa). M: magnetic peak; D: diamond peak. (**g**) The variation of the intensity ratio, $I(M2)/I(200)$, with pressure. The magnetic transition pressure (2.2 GPa) is obtained from fitting the data of $I(M2)/I(200)$

We conducted in situ synthesis of deuterium clathrate D_2–D_2O and monitored its stability as a function of pressure and temperature [14]. Deuterium clathrate was obtained under 2.2 kbar of D_2 pressure in the temperature range 200–270 K, and neutron data were collected during cooling from 200 to 40 K and during heating from 40 to 200 K at ambient pressure. We also used powdered ice (500 μm in diameter) instead of water as a source of D_2O, and our results showed that the formation of deuterium clathrate from ice powder is rapid due to its larger surface area and framework porosity (Fig. 15) [65]. The deuterium clathrates synthesized have sII structure (space group $Fd\bar{3}m$), and all the patterns were analyzed using the Rietveld method. The sII framework contains eight hexakaidecahedral ($6^4 5^{12}$) cages and 16 smaller dodecahedral (5^{12}) cages per unit cell. The number of D_2 molecules and their distribution in the cages vary sys-
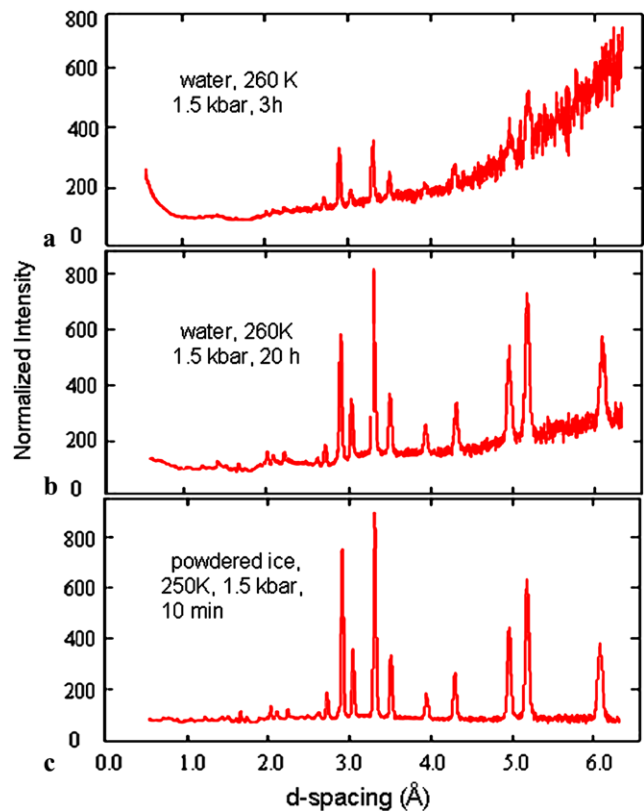

Fig. 15 Neutron diffraction patterns of deuterium clathrates produced from (*upper*, *middle*) water and (*lower*) powdered ice, at approximately the same P–T conditions. The formation kinetics of D_2-clathrates formed from ice powder is much faster than from water

tematically with temperature and pressure (Fig. 16). Below 50 K, the guest D_2 molecules are localized, with one D_2 occupying each small cage and four D_2 molecules in each large cage arranged in a tetrahedral geometry with a D_2–D_2 distance of 2.93(1) Å. Interestingly, the four D_2 molecules in the large cages are oriented towards the centers of the hexagons formed by the framework water molecules, presumably due to the energetic need of minimizing electrostatic repulsion. On the other hand, the distance between the four tetrahedrally arranged D_2 molecules (2.93 Å) is small—even shorter than that for solid hydrogen (3.78 Å) that was produced at extremely low temperatures and/or high pressures [67]. This D_2-densification behavior is striking and suggests a strong pressurizing effect (equivalent to about 16 kbar) that the clathrate framework exerts on the enclosed hydrogen. With increasing temperature, D_2 molecules become delocalized, as represented by a uniform distribution of their scattering densities on the surface of a sphere. Correspondingly, the number of D_2 in the large cage gradually decreases to 2.0(2) as temperature rises to 163 K at atmospheric pressure. In contrast, the occupancy of the small cage is constant at one D_2 molecule throughout the temperature range, which is believed to be required for stabilization of the clathrate structure. The clathrate structure
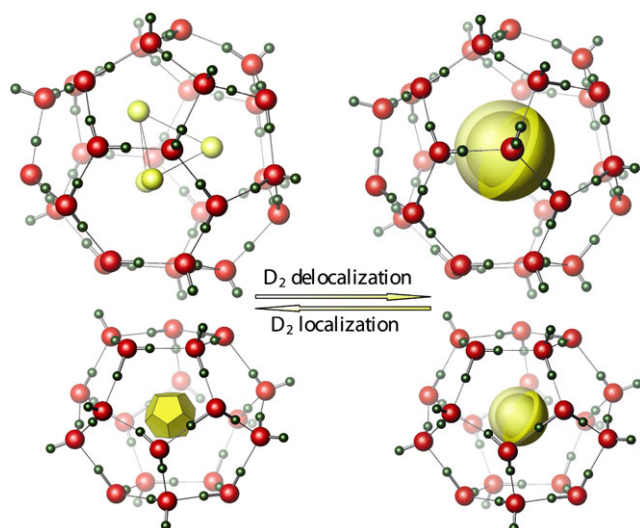
Fig. 16 Structural view of D_2 distribution in the large (*top*) and small (*bottom*) cages of deuterium clathrate. Oxygen atoms—*red spheres*; deuterium framework atoms—*green*; guest D_2 molecules—*yellow*. The $D_2 \cdots D_2$ separation is the distance between the centers of mass of the two D_2 molecules

tends to collapse as the D_2 starts to escape from the small cage. Upon cooling at 2 kbar, formation of the tetrahedral D_2 cluster in the large cage is complete at 180 K, consistent with the fact that increasing pressure stabilizes clathrate hydrates. Moreover, the distribution of the four D_2 molecules appeared to be similar to that at atmospheric pressure below 70 K when the maximum amount of D_2 was incorporated into the clathrate framework.

3.6 Hydrogen adsorption in MOFs

Metal–organic frameworks (MOFs) are nanoporous crystalline solids that are assembled by the connection of metal ions/clusters through organic molecular bridges [68]. Through systematic tuning of organic ligands and metal–oxygen clusters at various synthesis conditions, one may obtain framework types with various sizes and shapes of nanopores. Compared to aluminosilicate zeolites, MOFs are much lighter (with densities as low as 0.2 g/cm^3) and, in many cases, more porous (with specific surface areas of up to 4500–8000 m^2/g). Thus MOFs have a great potential for storage/separation of various gases such as hydrogen and CO_2. Despite intensive studies on MOFs during the past decade, further studies are still needed to unravel the mechanisms of gas uptake/release in these materials. In situ neutron scattering of MOFs with various pore sizes and shapes at different pressure/temperature conditions will be particularly useful.

We have recently conducted neutron diffraction experiments on $Cu_3[Co(CN)_6]_2$, a MOF compound, at 100 bar of D_2 from 40 to 200 K (Fig. 17) [13]. This compound is

a Prussian blue analogue (space group $Fm\bar{3}m$), in which 1/3 of the $[Co(CN)_6]^{3-}$ sites are vacant, resulting in an aperiodic system of nanopores throughout the structure (Fig. 17a). Rietveld analysis shows that the cell volume increases from 990.5(4) Å^3 under vacuum to 993.5(3) Å^3 at 100 bar both at 100 K, implying incorporation of significant amounts of D_2 into the nanoporous framework. Furthermore, difference Fourier nuclear density maps reveal that the D_2 molecules mainly occupy the interstitial (1/4, 1/4, 1/4) water sites (Figs. 17b and 17d) with some possibly associated with the exposed Cu cations (Fig. 17c). We have also synthesized and characterized another MOF, a highly stable lanthanide compound, Y(BTC) (BTC = 1,3,5-benzenetricarboxylate), which exhibits highly selective sorption for hydrogen over nitrogen gas [69]. Neutron diffraction provides direct structural evidence demonstrating that an optimal pore size (∼6 Å) strengthens the interactions between D_2 molecules with pore walls and allows for enhancing hydrogen adsorption from the interaction between hydrogen molecules with the pore walls rather than with the open metal sites within the framework. Moreover, some of the D_2–D_2 distances are as short as ∼2.86 Å, shorter than that in solid hydrogen. This behavior suggests a significant pressurizing effect of the MOF framework on the encapsulated D_2 molecules, also observed in hydrogen clathrate hydrate [13, 14].

4 Future perspective: LAPTRON

We have been proposing to construct a dedicated high-P high-T neutron beamline at LANSCE for research in Earth and material sciences. The proposed neutron instrument, named LAPTRON (Los Alamos Pressure–Temperature Research Opportunities with Neutrons), will be installed at flight path (FP)-8 in the Lujan Neutron Scattering Center. FP-8 is currently equipped with a chilled-H_2O moderator, Hg-shutter and beam stop; its short flight path will deliver high intensities to samples. The heart of LAPTRON is a large-volume 2000-ton hydraulic press, TAPLUS-2000 (Fig. 18). TAPLUS-2000 can accept several different modules loaded between the hydraulic ram and top plates. High temperature is achieved by resistive heating within the pressure cell.

Three devices will be available for LAPTRON, each with unique capabilities. The first is a toroidal type (Paris–Edinburgh) apparatus permitting a panoramic view of the sample and is thus well suited for diffraction studies of amorphous materials requiring large Q coverage, high pressures (up to 20 GPa) and high temperature (up to 2000°C). The second device will be a rotating anvil apparatus that can accept either Drickamer or Paris–Edinburgh assemblies. The device is placed between two sets of thrust bearings and harmonic drives that permit the sample to be rotated smoothly

Fig. 17 (**a**) Crystal structure of $Cu_3[Co(CN)_6]_2 \cdot 9H_2O$ at ambient condition (*brown*—Cu; *pink*—Co; *black*—C; *light blue*—N; *dark blue*—water). (**b**) Crystal structure of $Cu_3[Co(CN)_6]_2 \cdot nH_2$ (*green*—H_2) showing H_2 at the (1/4, 1/4, 1/4) site (the relatively *large green sphere* illustrates free-rotation of H_2 molecules in the cages). (**c, d**) Difference Fourier nuclear maps showing that the incorporated D_2 molecules mainly occupy the original water site (1/4, 1/4, 1/4) (**d**) with some possibly associated with Cu(C). The residual intensities at the Co and Cu sites are due to the limited resolution of our data and the strong scattering of Co and Cu
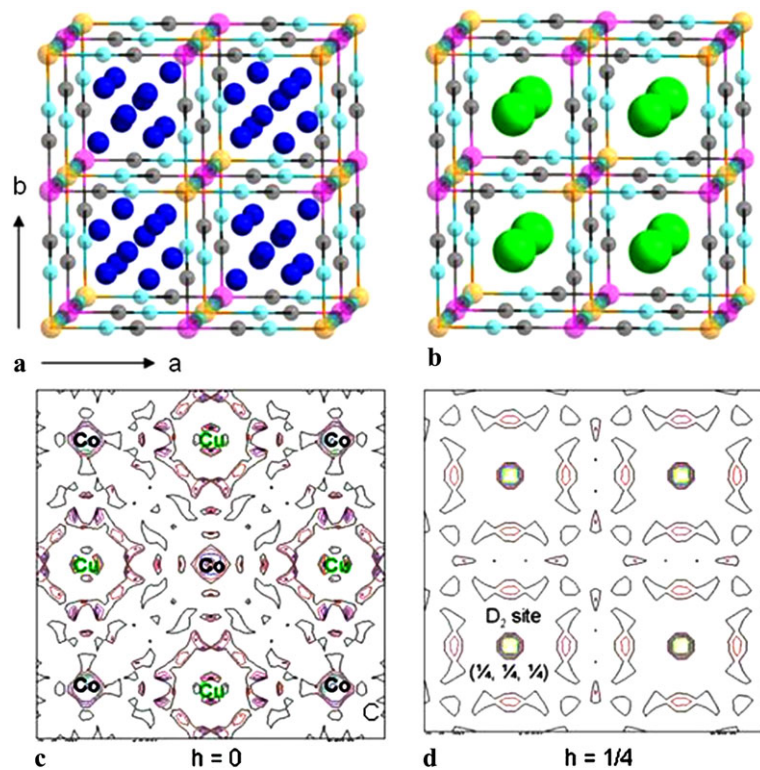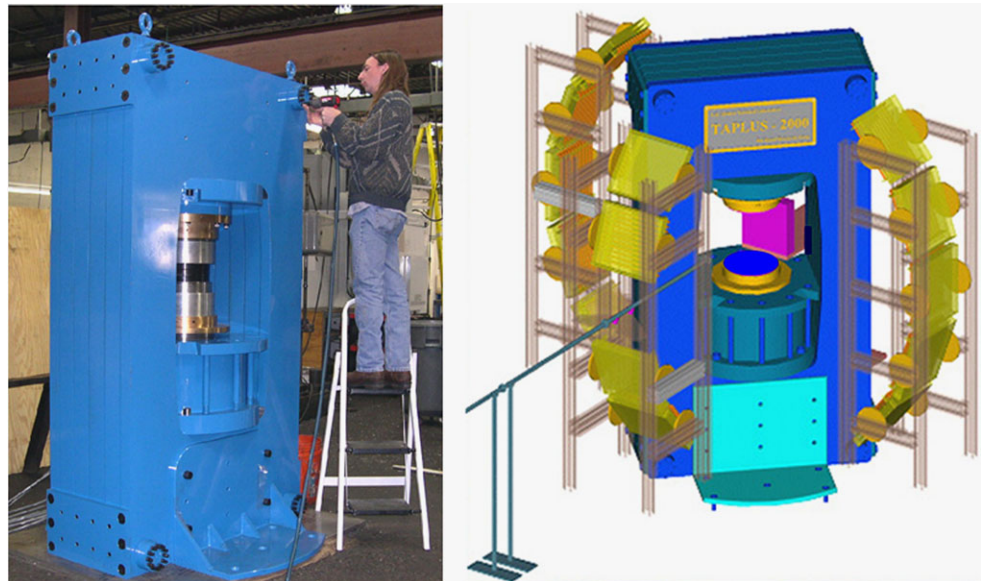

Fig. 18 *Left*, The 2000-ton press, TAPLUS-2000. *Right*, Schematic illustration of LAPTRON neutron diffraction and radiography set-up with TAPLUS-2000

under a load with an accuracy of $\pm0.01°$. Radiographs collected through 180° of rotation can be transformed into a 3D rendering of the sample at pressures up to 10 GPa and temperatures up to 2000°C with a spatial resolution of 10 μm or above. This device can also be used for simultaneous neutron diffraction and ultrasonic interferometry measurements. The third tool for LAPTRON will be a multi-anvil high-pressure deformation module, ZIA (Fig. 19). This system permits sample loading along three mutually perpendicular axes for controlled deformation up to 20% strain superimposed on pressures up to 20 GPa and temperatures up to 2000°C. The ZIA module has the advantage of building up higher pressures while maintaining anvil gaps for diffraction and radiographic windows. Simultaneous neutron diffraction and radiography using the scattered/transmitted neutrons are rendered possible by this geometry.

Successful implementation of LAPTRON will permit new experiments in neutron diffraction, thermal analysis,
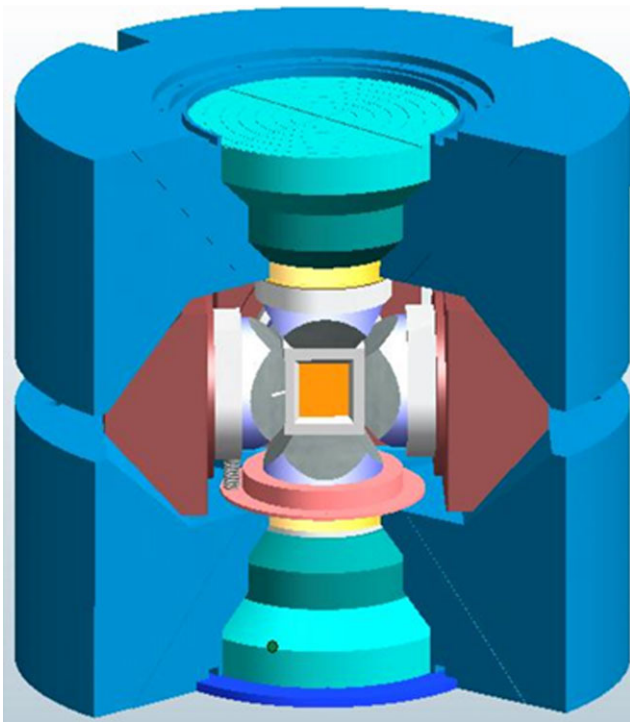
Fig. 19 ZIA (Z-Intrusion Anvil) deformation/pressure cubic anvil package, which will be loaded on a rotating apparatus with a hydraulic ram and a press frame

ultrasonic interferometry, neutron radiography, and computational tomography to be performed simultaneously at high-P–T conditions. It could provide a unique platform to address novel/challenging Earth and materials science problems in such areas as crystallization, texturing, amorphization, hydrogen bonding, and phase transformations. LAPTRON has recently been identified as one of the three high priority instrument platforms for development at Lujan Neutron Scattering Center of LANSCE and has gained its initial funding support from the University of California.

References

1. S.P. Kampermann, T.M. Sabine, B.M. Craven, R.K. Mcmullan, Acta Crystallogr. A **51**, 489 (1995)
2. B. Rupp, P. Fischer, E. Porschke, R.R. Arons, P. Meuffels, Physica C **156**, 559 (1988)
3. F.K. Larsen, P.J. Brown, M.S. Lehmann, M. Merisalo, Philos. Mag. B **45**, 31 (1982)
4. T. Steiner, W. Saenger, J. Am. Chem. Soc. **114**, 10146 (1992)
5. A.C. Lawson, J.A. Goldstone, J.G. Huber, A.L. Giorgi, J.W. Conant, A. Severing, B. Cort, R.A. Robinson, J. Appl. Phys. **69**, 5112 (1991)
6. H. Ptasiewiczbak, J. Leciejewicz, A. Zygmunt, J. Phys. F **11**, 1225 (1981)
7. J. Rodriguez-Carvajal, M.T. Fernandez-Diaz, J.L. Martinez, J. Phys., Condens. Matter **3**, 3215 (1991)
8. A. Krimmel, P. Fischer, B. Roessli, H. Maletta, C. Geibel, C. Schank, A. Grauel, A. Loidl, F. Steglich, Z. Phys. B **86**, 161 (1992)
9. A.M. Niraimathi, M. Hofmann, Phys. B **276–278**, 722 (2000)
10. J.M. DeTeresa, M.R. Ibarra, J. Garcia, J. Blasco, C. Ritter, P.A. Algarabel, C. Marquina, A. del Moral, Phys. Rev. Lett. **76**, 3392 (1996)
11. H. Xu, Y. Zhao, J. Zhang, D.D. Hickmott, L.L. Daemen, Phys. Chem. Miner. **34**, 223 (2007)
12. H. Xu, Y. Zhao, S.C. Vogel, L.L. Daemen, D.D. Hickmott, J. Solid State Chem. **180**, 1519 (2007)
13. Y. Zhao, H. Xu, L.L. Daemen, K. Lokshin, K.T. Tait, W.L. Mao, J. Luo, R.P. Currier, D.D. Hickmott, Proc. Natl. Acad. Sci. **104**, 5727 (2007)
14. K.A. Lokshin, Y. Zhao, D. He, W.L. Mao, H.-K. Mao, R.J. Hemley, Phys. Rev. Lett. **93**, 125503 (2004)
15. T. Proffen, S.J.L. Billinge, Appl. Phys. A **74**, S1770 (2002)
16. B. Palosz, E. Grzanka, S. Stel'makh, S. Gierlotka, R. Pielaszek, U. Bismayer, H.P. Weber, T. Proffen, W. Palosz, Diffus. Defect Data Part B **94**, 203 (2002)
17. A.N. Nikitin, W.A. Sukhoparov, J. Heinitz, K. Walther, High Press. Res. **14**, 155 (1995)
18. D. He, Y. Zhao, L.L. Daemen, J. Qian, K. Lokshin, T.D. Shen, J. Zhang, A.C. Lawson, J. Appl. Phys. **95**, 4645 (2004)
19. Y. Zhao, J. Zhang, B. Clausen, T.D. Shen, G.T. Gray III, L. Wang, Nano Lett. **7**, 426 (2007)
20. Y. Zhao, T.D. Shen, J. Zhang, Nano Res. Lett. **2**, 476 (2007)
21. Y. Zhao, J. Zhang, Appl. Phys. Lett. **91**, 201907-1-3 (2007)
22. Y. Zhao, J. Zhang, J. Appl. Crystallogr. **41**, 1095 (2008)
23. J.M. Besson, G. Hamel, T. Grima, R.J. Nelmes, J.S. Loveday, S. Hull, D. Häusermann, High Press. Res. **8**, 625 (1992)
24. J.M. Besson, R.J. Nelmes, G. Hamel, J.S. Loveday, G. Weill, S. Hull, Physica B **180–181**, 907 (1992)
25. J.M. Besson, S. Klotz, G. Hamel, T. Grima, I. Makarenko, R.J. Nelmes, J.S. Loveday, R.M. Wilson, W.G. Marshall, High Press. Res. **14**, 1 (1995)
26. Y. Le Godec, M.T. Dove, D.J. Francis, S.C. Kohn, W.G. Marshall, A.R. Pawley, G.D. Price, S.A.T. Redfern, N. Rhodes, N.L. Ross, P.F. Schofield, E. Schooneveld, G. Syfosse, M.G. Tucker, M.D. Welch, Mineral. Mag. **65**, 737 (2001)
27. J.S. Loveday, R.J. Nelmes, W.G. Marshall, R.M. Wilson, J.M. Besson, S. Klotz, G. Hamel, S. Hull, High Press. Res. **14**, 7 (1995)
28. R.B. Von Dreele, High Press. Res. **14**, 13 (1995)
29. S. Klotz, J.M. Besson, G. Hamel, R.J. Nelmes, J.S. Loveday, W.G. Marshall, R.M. Wilson, Appl. Phys. Lett. **66**, 1735 (1995)
30. S. Klotz, J.M. Besson, G. Hamel, R.J. Nelmes, J.S. Loveday, W.G. Marshall, High Press. Res. **14**, 249 (1996)
31. Y. Zhao, R.B. Von Dreele, J.G. Morgan, High Press. Res. **16**, 161 (1999)
32. Y. Zhao, D. He, J. Qian, C. Pantea, K.A. Lokshin, J. Zhang, L.L. Daemen, *Frontiers of High Pressure Research* (Elsevier, New York, 2005), pp. 461–474
33. K.A. Lokshin, Y. Zhao, Rev. Sci. Instrum. **76**, 1 (2005)
34. J.B. Parise, K. Leinenweber, D.J. Weidner, K. Tan, R.B. Vondreele, Am. Mineral. **79**, 193 (1994)
35. Y. Zhao, A.C. Lawson, J. Zhang, B.I. Bennett, R.B. Von Dreele, Phys. Rev. B **62**, 8766 (2000)
36. K. Bennett, R.B. Von Dreele, H.R. Wenk, in Fifteenth Meeting of the International Collaboration on Advanced Neutron Sources, ICANS-XV, Tsukuba, Japan, 6–9 Nov. 2000, (2000), vol. 1, p. 473
37. H.R. Wenk, L. Lutterotti, S. Vogel, Nucl. Instrum. Methods Phys. Res. A **515**, 575 (2003)

38. S.C. Vogel, C. Hartig, L. Lutterotti, R.B. Von Dreele, H.R. Wenk, D.J. Williams, Powder Diffr. **19**, 65 (2004)
39. L.G. Khovstantsev, L.F. Vereshchagin, A.P. Novikov, High Temp. High Press. **9**, 637 (1977)
40. Y. Ding, J. Xu, C.T. Prewitt, R.J. Hemley, H.K. Mao, J. Zhang, J. Qian, S.C. Vogel, K. Lokshin, Y. Zhao, Appl. Phys. Lett. **86**, 052505 (2005)
41. A.N. Ivanov, D.F. Litvin, B.N. Svenko, L.S. Smirnov, V.I. Voronin, A.E. Teplykh, High Press. Res. **14**, 209 (1995)
42. J.D. Jorgensen, S. Pei, P. Lightfoot, D.G. Hinks, B.W. Veal, B. Dabrowski, A.P. Paulikas, R. Kleb, I.D. Brown, Physica C **171**, 93 (1990)
43. O. Yamamuro, K. Okishiro, T. Matsuo, T. Ohta, Y. Kume, R.M. Ibberson, Physica B **241–243**, 466 (1997)
44. F.K. Katsaros, T.A. Steriotis, K.L. Stefanopoulos, N.K. Kanellopoulos, A.Ch. Mitropoulos, M. Meissner, A. Hoser, Physica B **276–278**, 901 (2000)
45. Z. Budrovic, H. Van Swygenhoven, P.M. Derlet, S. Van Petegem, B. Schmitt, Science **304**, 273 (2004)
46. E.O. Hall, Proc. Phys. Soc. Lond., Sect. B **64**, 747 (1951)
47. N.J. Petch, J. Iron Steel Inst. **174**, 25 (1953)
48. M.F. Ashby, Philos. Mag. **21**, 399 (1970)
49. M.F. Ashby, D.R. Jones, *Engineering Materials* 2: *An Introduction to Microstructures. Processing and Design* (Pergamon, Oxford, 1986), p. 369
50. T.D. Shen, R.B. Schwarz, S.H. Feng, J.G. Swadener, J.Y. Huang, M. Tang, J. Zhang, S.C. Vogel, Y. Zhao, Acta Mater. **55**, 5007 (2007)
51. J. Zhang, Y. Zhao, Y. Wang, L.L. Daemen, J. Appl. Phys. **103**, 093513-1-4 (2008)
52. C.T. Prewitt, J.B. Parise, Rev. Mineral. Geochem. **41**, 307 (2000)
53. C. Meade, R. Jeanloz, Geophys. Res. Lett. **17**, 1157 (1990)
54. A. Pavese, M. Catti, G. Ferraris, S. Hull, Phys. Chem. Miner. **24**, 85 (1997)
55. M.B. Kruger, Q. Williams, R. Jeanloz, J. Chem. Phys. **91**, 5910 (1989)
56. S. Raugei, P.L. Silvestrelli, M. Parrinello, Phys. Rev. Lett. **83**, 2222 (1999)
57. J.B. Parise, K. Leinenweber, D.J. Weidner, K. Tan, Am. Mineral. **79**, 193 (1994)
58. T. Yagi, T. Suzuki, S.-I. Akimoto, J. Geophys. Res. **90**, 8784 (1985)
59. Q. Guo, H.-K. Mao, J. Hu, J. Shu, R. Hemley, J. Phys., Condens. Matter **14**, 11369 (2002)
60. T. Okamoto, T. Fuji, Y. Hidaka, E. Hiroshima, J. Phys. Soc. Jpn. **23**, 1174 (1967)
61. R.W. Vaughan, H.G. Drickamer, J. Chem. Phys. **47**, 1530 (1967)
62. Y. Ding, Y. Ren, P. Chow, J. Zhang, S.C. Vogel, Y. Xu, Y. Zhao, H.-K. Mao, Phys. Rev. B **74**, 144101-1-4 (2006)
63. D. Bloch, F. Chaissé, R. Pauthenet, J. Appl. Phys. **37**, 1401 (1966)
64. Y. Tokura, N. Nagaosa, Science **288**, 462 (2000)
65. K.A. Lokshin, Y. Zhao, Appl. Phys. Lett. **88**, 13109-1-3 (2006)
66. S. Bobev, K.T. Tait, Am. Mineral. **89**, 1208 (2004)
67. S.N. Ishmaev, I.P. Sadikov, A.A. Chernyshov, B.A. Vindryaevskii, V.A. Sukhoparov, A.S. Telepnev, G.V.J. Kobelev, Exp. Theor. Phys. **84**, 394 (1983)
68. J.L.C. Rowsell, O.M. Yaghi, Angew. Chem., Int. Ed. **44**, 4670 (2005)
69. J. Luo, H. Xu, Y. Liu, Y. Zhao, L.L. Daemen, C. Brown, T.V. Timofeeva, S. Ma, H.-C. Zhou, J. Am. Chem. Soc. **130**, 9626 (2008)